Development of a multivariate spectral emissivity model for an advanced high strength steel alloy through factorial design-of-experiments

Fatima K. Suleiman*, Kaihsiang Lin, Kyle J. Daun

Department of Mechanical and Mechatronics Engineering, University of Waterloo

200 University Avenue West, Waterloo, Ontario N2L 3G1, Canada

Highlights

- Spectral emissivity model for a steel alloy using response surface methodology

- Used for improving three-wavelength pyrometry

- Accounts for dew point, alloy composition, pre-annealed surface state, wavelength

- Roughness and alloy composition dominate at long and short wavelengths respectively

- Dew point is a weak main effect, but strongly interacts with alloy composition

*Corresponding author: fsuleiman@uwaterloo.ca

Development of a multivariate spectral emissivity model for an advanced high strength steel alloy through factorial design-of-experiments

Fatima K. Suleiman*, Kaihsiang Lin, Kyle J. Daun

Department of Mechanical and Mechatronics Engineering, University of Waterloo

200 University Avenue West, Waterloo, Ontario N2L 3G1, Canada

*Corresponding author: fsuleiman@uwaterloo.ca

Abstract

Variations in the spectral emissivity of advanced high strength steels (AHSS) during intercritical annealing leads to errors in pyrometry measurements, which, in turn, cause thermal excursions that impact the mechanical properties of the steel. This paper presents an empirical approach for modelling the spectral emissivity of advanced high strength steel. Samples of two dual-phase steel (DP980) alloys, having Si/Mn ratios of 0.04 and 0.23, are heated within a galvanizing simulator in atmospheres of 95%/5% N_2/H_2 and dew points of 10°C and −30°C. The spectral hemispherical reflectance of the annealed samples was measured with an FTIR spectrometer. The variation of the spectral emissivity with dew point, alloy composition, pre-annealed surface state, and wavelength is analyzed using full factorial designs. The significant main and interaction effects vary across the spectral range, with the ratio of alloy components and pre-annealed surface state dominating at shorter and longer wavelengths, respectively. The predicted spectral emissivity values obtained from the model fitted for a three-channel pyrometer shows good agreement with the measurements. This study shows response surface methods (RSM) to be a viable approach for developing spectral emissivity models for pyrometry applications.

1. Introduction

With strict global regulations surrounding vehicle emission and crash performance, automotive manufacturers increasingly rely upon the superior mechanical characteristics of advanced high strength steel (AHSS) alloys for lightweighting, in order to improve fuel economy without sacrificing strength and formability. Achieving the desired mechanical properties is contingent on precisely controlling the steel temperature during processing using feedback from pyrometers at critical process locations, e.g. within the annealing furnace. Accurate pyrometry requires detailed knowledge of the spectral emittance of the steel, which is known to vary with the as-received state of the coil and evolves during annealing due to oxidation. Pyrometry errors associated with imperfectly-known emissivity cause temperature excursions during processing, which, in turn, lead to substandard mechanical properties that cost steelmakers millions of dollars annually [1].

Many methods have been developed to mitigate pyrometer errors caused by uncertain spectral emissivity [2-7]. Whenever possible, pyrometers are aimed at the notch formed between the steel strip and the roll to exploit the blackbody cavity effect [2]. Unfortunately, this method is sensitive to misalignment and any temperature difference between the strip and the roll; moreover, many key points in steel production do not facilitate this type of measurement. Dual- and multi-spectral measurements are also often used to mitigate the impact of uncertain radiative properties [3-7]. In two-color pyrometry (a version of dual-spectral pyrometry), the ratio of the spectral emissivity at the two detection wavelengths is assumed to be constant and known. In the case where the radiative properties are taken to be independent of wavelength, i.e. the greybody assumption, this ratio is unity [5]. While the ratio method is resilient to partially-filled field-of-views and atmospheric attenuation if both detection wavelengths are equally attenuated, it does not address the fact that the spectral emissivity ratio varies with the evolving surface state of the strip. For multi-wavelength methods, spectral irradiance measurements at three or more discrete wavelengths are combined with an emissivity compensation algorithm to infer the surface temperature [6,7]. This captures the complex wavelength-dependent variations in emissivity, thereby overcoming some of the limitations involved with assuming constant emissivity and grey surfaces in the case of single and dual-wavelength pyrometry, respectively. However, the accuracy of the temperature estimate strongly depends on the ability of the emissivity function to capture the spectral changes produced by the evolving surface state, while avoiding over-tuning that may occur for functions having too many degrees-of-freedom.

Several experimental and theoretical studies have been conducted to understand and model the varying spectral emissivity of several materials [8-12]. Khan et al. [8, 9] used linear and log-linear polynomials to develop wavelength-dependent emissivity models for platinum, chromium, molybdenum, and iron, based on experimental data extracted from the published literature. Pellerin et al. [10, 11] produced an emissivity compensation algorithm for aluminum alloys based on the Hagen-Rubens relation [13] to explicitly account for both wavelength- and temperature-dependent variations. Duvaut et al. [12] compared the performance of several mathematical and physical emissivity compensation algorithms for steel, aluminum, tantalum, and titanium at 573 K, and wavelengths between 2 to 10 micrometers. They considered linear and fractional wavelength-dependent models, as well as relationships developed from the Maxwell and Fresnel's equations. While these models are robust for uncontaminated surfaces, they are unreliable for materials whose emissivity varies significantly with factors other than wavelength and temperature, e.g. surface roughness or the formation of a surface oxide [3].

Despite the known effects of surface roughness, alloy composition, dew point, and oxide film thickness on spectral emissivity [14, 15], very few studies have reported multivariable emissivity relationships that account for these additional parameters. Iuchi et al. [16] derived an emissivity model that considers oxide film growth on metal surfaces by expressing the directional and polarized emissivities as functions of direction, oxide film thickness, and optical constants of the metal and the oxide film. Wen [17] used the Agababov roughness function [18] to update four existing compensation algorithms to model the effects of surface roughness on the spectral emissivity of aluminum alloys. King et al. [19] and Jo et al. [20] used a modified geometric optics approximation (GOA) to obtain directional spectral emissivity models for metal surfaces that account for dependencies on temperature, composition, and roughness. Lin and Daun [21] applied the Davies' model [22] to investigate the relationship between surface roughness and spectral emissivity for dual-phase AHSS alloys.

In this paper, factorial design of experiments is proposed as a statistical tool for modelling the interdependent effects of wavelength, alloy composition, annealing atmosphere, and pre-annealed surface state on the spectral emissivity of dual-phase AHSS alloys. To the best of our knowledge, this is the first time factorial designs have been used to develop spectral emissivity models for pyrometry during metallurgical processing. The analysis considers coupons cut from coils of two different cold-

rolled DP980 alloys, with silicon-to-manganese (Si/Mn) ratios of 0.23 and 0.04 respectively. Coupons are either left in their as-received state or mechanically-polished. The coupons are then annealed in a 95% N_2/5% H_2 atmosphere at dew points of -30°C or 10°C, within a galvanizing simulator. The spectral emittance of each sample is obtained from reflectance measurements made with a Bruker Invenio-R FTIR spectrometer (1.2 μm – 25 μm), but only the measurements for the infrared pyrometry range of 1.2 μm – 4.0 μm is analyzed in this paper.

The most significant main and interaction effects were determined through an analysis of variance (ANOVA) procedure. The pre-annealed surface state of the steel is the most dominant effect at longer wavelengths, while alloy composition dominates at shorter wavelengths. Also, while the annealing atmosphere dew point does not strongly affect the varying emissivity, its interaction effect with alloy composition contributes significantly to the observed variations, especially for wavelengths below 3 μm. These effects were then incorporated into a bilinear model with parameters derived through regression to the experimental data. The fitted linear regression model obtained for a three-wavelength pyrometer (1.6 μm, 2.1 μm, 2.4 μm) provides a good approximation of the experimental measurements (R^2 =0.98).

The results demonstrate how factorial designs provides key insights into the relationship between the surface state and radiative properties of the steel strip, and may be used to develop multivariable emissivity compensation algorithms for pyrometry. While this paper focuses on intercritical annealing of dual-phase steels, the methodology is generally applicable to any other type of material or process.

2. Experimental Procedure and Analysis Methodology

2.1 Sample Preparation and Processing

Coupons were cut from coils of cold-rolled DP980 steel, having alloy compositions that conform to ASTM A1079-17 as detailed in Table 1. Although the exact alloy composition is proprietary, the Si/Mn mass ratios, which have the most pronounced effect on oxide composition, are 0.04 and 0.23, as measured by spark atomic emission spectrometry. In order to investigate the influence of the pre-annealed surface state on the spectral emissivity, half of the coupons were polished using a series of polishing wheels with progressively finer grit and particle size (240grit SiC, 320grit

SiC, 400 grit SiC, 600 grit SiC), producing a mirror-like finish. The root-mean-square (RMS) roughness for all the samples was measured using an optical profilometer (WYKO NT1100). The sub-group of polished surfaces has an RMS roughness of $R_q = 0.15$ μm, while the as-received subgroup has an RMS roughness of $R_q = 0.65$ μm. All the samples were annealed within a galvanizing simulator (MGS, Iwatani-Surtec, Japan) [23] with a 95%/5% N_2/H_2 atmosphere according to the heating schedule illustrated in Figure 1. The samples are rapidly quenched to freeze their high-temperature surface state for *ex situ* characterization of the corresponding radiative properties. Given that spectral emissivity is primarily a surface property, the rapid quench ensures that *ex situ* measurements are an approximate representative of the samples' high-temperature surface state. Similarly, previous pyrometry studies on steel alloys [6,11] indicate that observed variations in emissivity at high temperatures are significantly influenced by the changes in surface properties due to oxidation and the resulting interference effect. Nevertheless, potential variations in emissivity due to temperature-dependent changes in electrical conductivity are also discussed later in this paper. The annealing dew point for each sample is listed in Table 2. Two coupons were processed for each experimental condition in order to provide a measure of repeatability. All samples were cleaned and rinsed with ethanol and acetone before annealing and again prior to making radiative measurements post-annealing.

The near-normal directional-hemispherical spectral reflectance, ρ_λ, of each annealed coupon was measured using a Bruker Invenio-R FTIR spectrometer (1.2 μm - 25 μm), but only the measurements in the infrared pyrometry range of 1.2 μm - 4 μm are used for this study. The FTIR has a calibration uncertainty of ±2% and a repeatability accuracy of less than ±1% based on reflectance measurements over the entire spectrum. The near-normal emissivity, ε_λ, was then inferred using Kirchhoff's law [24]

$$\varepsilon_\lambda = 1 - \rho_\lambda \tag{1}$$

These spectral emissivity measurements from the annealed coupon are then combined with the pre-annealed material properties (Si/Mn ratio and surface state) and the process parameter (dew point) to develop a multivariate emissivity compensation relationship using the response surface methodology described in the next section.

Table 1. Nominal chemical composition of DP980 [25].

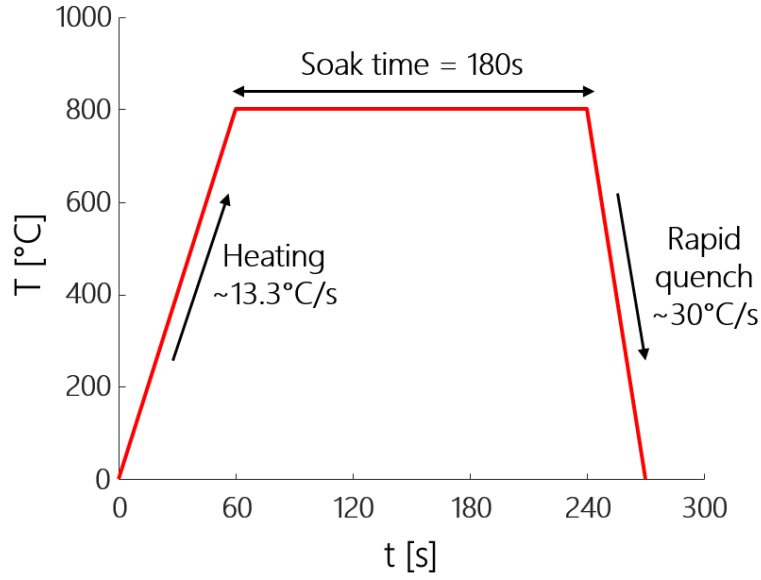| Constituents	C	P	S	Mn+Al+Si	Cu	Ni	Cr+Mo	V+Nb+Ti
%mass max	0.23	0.08	0.015	6.00	0.20	0.50	1.40	0.35

Figure 1. Schematic illustration of the annealing schedule for the tested coupons.

Table 2. List of annealed coupons indicating the dew point of the annealing atmosphere, the ratio of alloy components, and the pre-annealed surface state.

Sample/Run No.	Dew Point	Si/Mn Ratio	Surface State
1	-30°C	0.04	Polished
2	-30°C	0.04	As-received
3	-30°C	0.23	Polished
4	-30°C	0.23	As-received
5	+10°C	0.04	Polished
6	+10°C	0.04	As-received
7	+10°C	0.23	Polished
8	+10°C	0.23	As-received

2.2   Response Surface Methodology (RSM): Factorial Design

In the response surface methodology, variations in the response variable, or a set of response variables, can be related to the combined influence of several independent variables. These independent variables are called *factors* [26]. A common RSM technique is the factorial design of experiments, where all levels of one factor are efficiently combined with all levels of the other factors [27]. The *level* of a factor refers to the value held by the independent variable during an experiment. Factorial designs provide an estimate of the main and interaction effects, which are important when investigating how the joint effects of the process factors contribute to the observed changes in the response (dependent variable). The *effect* of a factor refers to the change in the response variable due to a change in the level of the factor [26]. A *main effect* describes the influence of a factor on the response irrespective of the levels of the other factors, while an *interaction effect* considers the influence a factor has on the response variable in the context of the level of another factor [26]. An interaction effect becomes significant when the effect of one factor on the dependent variable varies with the level of another factor.

The observations from a factorial design can be modelled by a fixed effects model if the levels of the factors (i.e. values of the independent variables) are assumed to be constant [26]. Once the model structure is defined, an analysis of variance (ANOVA) procedure is carried out to identify the factors and factor interactions that have the most significant effects on the response. ANOVA models can be explicitly translated into an equivalent linear regression model [26, 28-30], so a factorial design analysis also produces functions that elucidate the relationship between the factors and their response.

In this study, factorial designs are used to analyze the spectral emissivities of the annealed samples in two stages. First, individual 2^3 full factorial designs are used to evaluate the spectral emissivity measured for all samples, at discrete pyrometry detection wavelengths of 1.2 μm, 1.6 μm, 2.1 μm, 2.4 μm, 2.8 μm, 3.2 μm, 3.6 μm, and 4.0 μm. This is done to investigate how the dew point, Si/Mn ratio, and pre-annealed surface state (polished vs. unpolished), labelled "A", "B", and "C", respectively, interact to produce variations in the radiative properties without considering the role of wavelength. These factors each have two levels, as shown in Table 2. In the second stage, a general full factorial design is carried out by adding a factor for wavelength ("D"), which accounts for the spectral variation of the properties. Factor D has three-levels: 1.6 μm, 2.1 μm, and

2.4 µm; corresponding to the detection wavelengths for a commercial multi-wavelength pyrometer (Williamson PRO MWX-ST-17).

==To facilitate comparison of the main and interaction effects, the factor levels are converted to dimensionless coded values using Eq. (2) [26]:==

$$\text{coded level} = \frac{2 \times \left(\text{uncoded level} - \text{mean} \right)}{\text{range}} \tag{2}$$

The significance of the effects of dew point, Si/Mn ratio, surface state, wavelength, and their interactions on the spectral emissivity of the DP980 steel is determined using an ANOVA procedure at a 95% confidence interval (CI). The regression model for predicting the spectral emissivity is then constructed using only the statistically significant model terms identified from the ANOVA results for the general factorial design.

Table 3. Factors Dew point ("A"), Si/Mn Ratio ("B"), Surface State ("C"), and Wavelength ("D"), with their uncoded and coded levels.

Factors	Uncoded Levels	Coded Levels
Dew Point (A)	-30°C	-1
	+10°C	+1
Si/Mn Ratio (B)	0.04	-1
	0.23	+1
Surface State (C)	Polished ($R_q = 0.15$ µm)	-1
	As-received ($R_q = 0.65$ µm)	+1
Wavelength (D)	1.6 µm	-1.083
	2.1 µm	0.166
	2.4 µm	0.917

3. Results and Discussion

3.1 Spectral Emissivity Measurements

Figure 2 shows the spectral emissivity of the annealed DP980 alloys. Each curve represents the average of the two measurements from replicate samples. The standard deviation between the measurements from the two replicates ranges between 8.4×10^{-8} and 0.02, with a mean value of 0.005 (i.e. a mean relative standard deviation of 1.3%), demonstrating that the measurements are repeatable. Generally, the spectral emissivity for all samples decreases with increasing wavelength as expected for metals within the infrared spectrum.

The spectral emissivity for the polished samples in Figure 2 (a) shows greater variability in comparison to the as-received samples in Figure 2 (b). Typically, the spectral emissivity of a material increases with increasing roughness in the context of EM wave scattering theory [24, 31] but from the polished samples in Figure 2 (a), it is observed that for the shorter wavelengths (<~2 μm), the emissivity values are higher than their as-received counterparts in Figure 2 (b). This contrary relationship between surface roughness and spectral emissivity is attributed to the interference effect of coherent reflection in the presence of a uniform oxide layer on the annealed surfaces [32]. The absence of large scale roughness on the polished surfaces allows for a more uniform oxide layer to form during the annealing process [33]. The spectral emissivity at shorter wavelengths is influenced by the structure and uniformity of the oxide layer formed during the annealing process, which depends on the pre-annealed surface state of the steel.

Scanning electron micrographs (SEM) of the annealed low Si/Mn ratio coupons, shown in Figure 3, highlights the different oxide structures that contribute to the varying spectral emissivity. Figure 3 (a) and (b) reveal a uniform fully developed oxide layer is formed for the polished samples. For the polished specimen annealed at -30°C, shown in Figure 3 (a), the oxide layer appears homogenous, while the polished sample annealed at the higher dew point (Figure 3 (b)) shows a thicker oxide layer with a few oxide nodules. On the other hand, Figures 3 (c) and (d) show that the as-received samples form isolated oxide nodules instead of a continuous oxide layer. The amount of oxide nodules formed on the as-received surfaces appears to increase with increasing dew point, as seen in Figure 3 (d). The lack of a visible oxide layer on the as-received samples is most probably due to the fracture artifacts introduced by the cold-rolling process. The

removal of these artifacts, pre-annealing, appears to promote the formation of a fully-developed, homogeneous oxide layer on the polished samples.

Figure 2 (a) and (b) also show that samples with lower Si/Mn ratios generally have higher spectral emissivity values. Increasing the dew point causes the emissivity to increase for samples with the lower Si/Mn ratio, while the opposite effect is observed for the higher Si/Mn ratio. The former effect is caused by the segregation of alloying elements from the bulk material to form selective oxides on the surface during annealing. Changes in the surface topography caused by these oxides lead to variations in the spectral emissivity [14, 34]. The Ellingham diagram indicates that the most likely oxides to form are MnO, SiO_2, $MnSiO_3$, Mn_2SiO_4 [35], but given the higher solubility of MnO in austenite (7.2 $(ppm)^2$) relative to the other oxides ($SiO_2 = 3.1 \times 10^{-5}$ $(ppm)^3$, $MnSiO_3 \approx Mn_2SiO_4 = 7.6 \times 10^{-6}$ $(ppm)^7$) [36] combined with the lower Si/Mn ratio, and higher oxygen pressure, for the alloys considered here, the oxides are expected to be almost exclusively MnO [37]. This means that samples with more manganese content (i.e. lower Si/Mn ratio) are more likely to exhibit higher spectral emissivity during annealing because they have a greater tendency to oxidize. Overall, these results indicate that the radiative properties of dual-phase alloys depend not only on annealing atmosphere and alloy composition but also on their pre-annealed surface states.
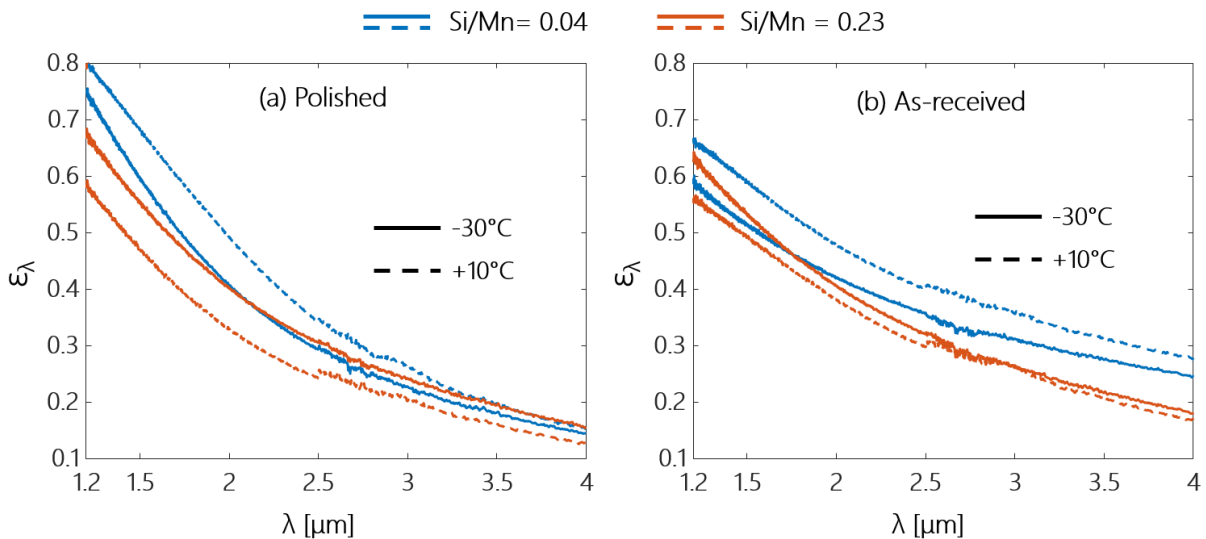

Figure 2. Measured spectral emissivity, ε_λ for (a) polished samples (b) as-received samples.
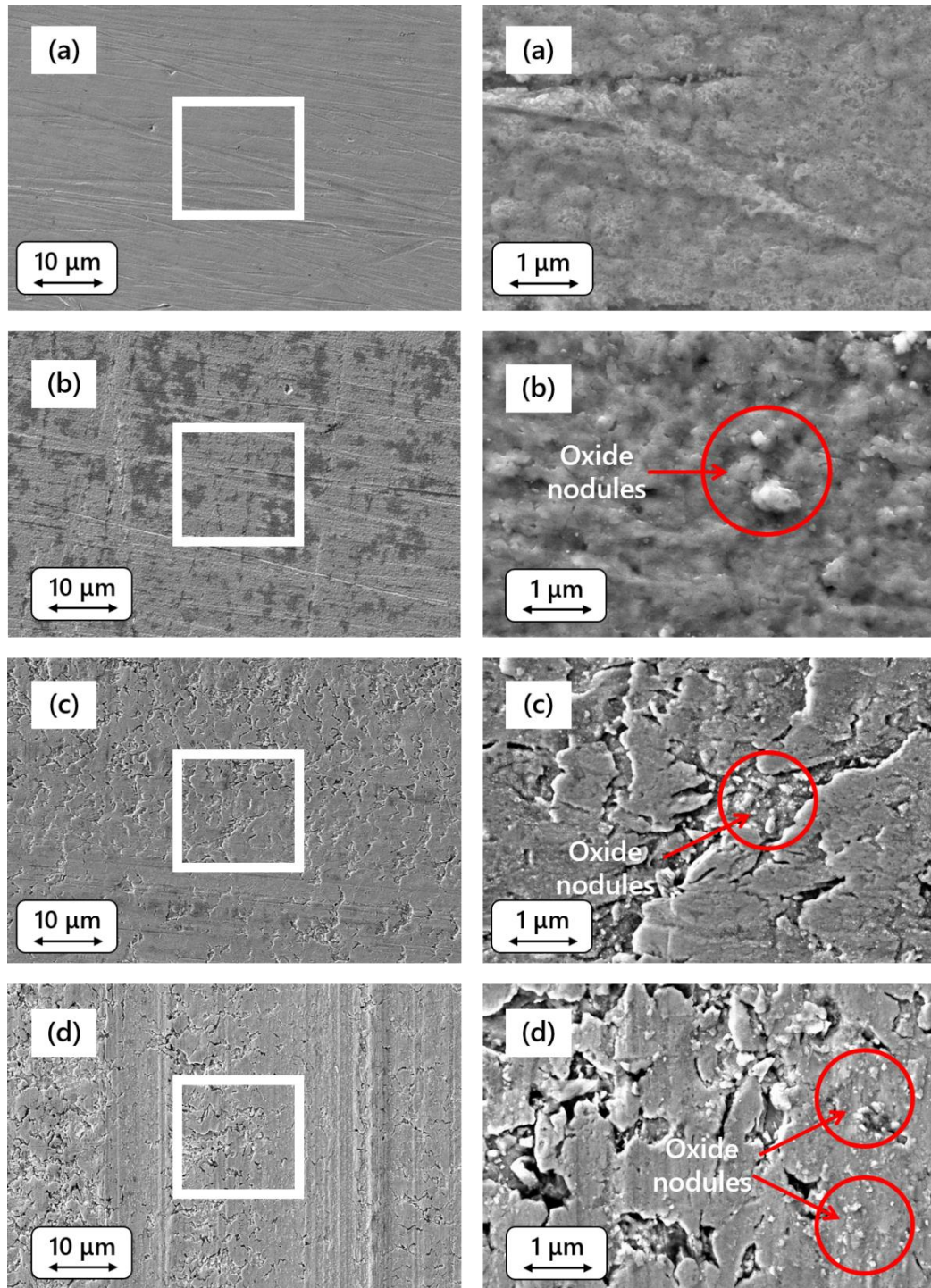
Figure 3. Scanning electron micrographs (SEM) of the annealed low Si/Mn ratio samples. The images on the right corresponds to the white boxed region in the image on the left. (a) Si/Mn=0.04, polished, annealed at -30°C, (b) Si/Mn=0.04, polished, annealed at +10°C (c) Si/Mn=0.04, as-received, annealed at -30°C, and (d) Si/Mn=0.04, as-received, annealed at +10°C.

3.2 2^3 full factorial design

The 2^3 factorial design matrix and the spectral emissivity measurements from both replicates are shown in Table 4. The run order of the experiment was randomized to protect the analysis from serially-correlated errors as well as the effects of unknown nuisance variables.

The ANOVA procedure is applied to determine not only the factors and interactions that are significant but also the magnitude of these effects as expressed by the percentage contribution of their sum-of-squares residual relative to the total sum-of-squares residual. This provides an approximate quantitative measure of the main and interaction effects responsible for the varying spectral emissivity. Figure 4 summarizes the percent contribution of effects across the spectral range, while detailed ANOVA results at each of the eight wavelengths are included as supplemental material to this paper. The contributions of the main and interaction effects vary significantly with different trends across the wavelengths. The main effect of Si/Mn ratio (B) dominates at shorter wavelengths ($\lambda < \sim2.6$ μm), accounting for up to 51% at its peak wavelength of 2.1 μm, whereas the main effect of surface state (C) dominates at the longer wavelengths. The results also indicate that the emissivity is insensitive to the main effect of dew-point, accounting for a maximum of 1.24% of the variability at 2.1 μm. However, the interaction between dew point and Si/Mn ratio (AB) is the most significant interaction effect, meaning that the impact of dew-point depends strongly on the alloy composition of the steel. The most prominent effects over this spectral range are, in order of importance: Si/Mn ratio (B), surface state (C), dew point-Si/Mn ratio (AB) interaction, and Si/Mn ratio-surface state (BC) interaction; these four effects combined account for over 93% of the total variability observed in the spectral emissivity.

A statistical F-test is carried out to evaluate the significance of the effects at a level of 0.05, corresponding to a 95% confidence interval (F-value $> F_{(0.05,1,8)} = 5.32$). The results of this test, summarized in Table 5, shows that the four factors identified via the magnitude of their percent contributions are significant at all wavelengths. Some of the main and interaction effects with minimal contributions to the total variability (less than 4%) were identified to be statistically significant via the F-test. All main and interaction effects were found to be statistically significant at 1.6 μm, while the specific significant effects vary across the other pyrometry wavelengths. A detailed analysis of the main effects and interaction effects at the selected pyrometry wavelengths is provided in Appendix A and Appendix B, respectively. Overall, both the estimated percent

contributions and the F-test results show that the key main and interaction effects that contribute to the change in spectral emissivity vary with wavelength. This observation provides a foundation for analyzing and optimizing wavelength combinations for improving the reliability of pyrometry estimates. For future pyrometer design, the RSM process can be used to estimate the sensitivity of selected wavelengths to key process effects and to understand how this sensitivity varies among the wavelengths. Applying this procedure will facilitate the selection of wavelengths that will provide the most sensitivity to the varying emissivity and thus minimize the error in the pyrometrically-inferred temperature.

Table 4: The 2^3 factorial design matrix and spectral emissivity responses

| Std. No.	Run No.	Coded Factors			Spectral emissivity, ε_λ at selected pyrometry wavelengths							
		A	B	C	1.2 μm	1.6 μm	2.1 μm	2.4 μm	2.8 μm	3.2 μm	3.6 μm	4.0 μm
					Replicate I							
1	1	-1	-1	-1	0.754	0.547	0.375	0.308	0.249	0.205	0.172	0.147
2	5	1	-1	-1	0.808	0.644	0.461	0.370	0.284	0.231	0.188	0.154
3	3	-1	1	-1	0.670	0.527	0.385	0.326	0.267	0.224	0.188	0.160
4	7	1	1	-1	0.586	0.438	0.311	0.258	0.218	0.178	0.148	0.123
5	2	-1	-1	1	0.588	0.485	0.398	0.361	0.315	0.289	0.266	0.242
6	6	1	-1	1	0.662	0.561	0.455	0.408	0.370	0.332	0.300	0.270
7	4	-1	1	1	0.621	0.502	0.382	0.333	0.285	0.241	0.212	0.183
8	8	1	1	1	0.552	0.465	0.359	0.306	0.277	0.236	0.198	0.168
					Replicate II							
1	1	-1	-1	-1	0.752	0.557	0.383	0.312	0.249	0.202	0.168	0.142
2	5	1	-1	-1	0.803	0.638	0.456	0.365	0.287	0.228	0.185	0.152
3	3	-1	1	-1	0.663	0.511	0.371	0.313	0.259	0.213	0.181	0.153
4	7	1	1	-1	0.570	0.431	0.302	0.253	0.221	0.185	0.150	0.125
5	2	-1	-1	1	0.583	0.499	0.412	0.375	0.330	0.299	0.271	0.251
6	6	1	-1	1	0.661	0.571	0.464	0.416	0.379	0.342	0.311	0.279
7	4	-1	1	1	0.627	0.506	0.386	0.335	0.278	0.237	0.204	0.178
8	8	1	1	1	0.560	0.476	0.366	0.315	0.269	0.231	0.194	0.164
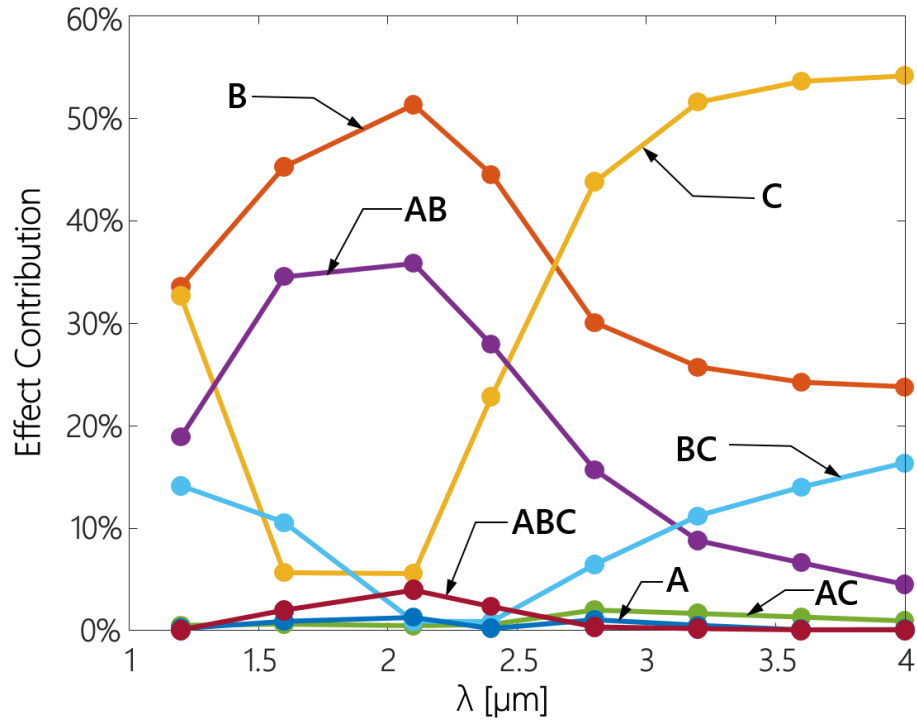
Figure 4. Percent contribution of the main and interaction effects for wavelengths: 1.2 μm, 1.6 μm, 2.1 μm, 2.4 μm, 2.8 μm, 3.2 μm, 3.6 μm, and 4.0 μm.

Table 5: Statistically significant factors identified from the F-test at 95% confidence interval

Source	Wavelength							
of variation	1.2 μm	1.6 μm	2.1 μm	2.4 μm	2.8 μm	3.2 μm	3.6 μm	4.0 μm
A	✓	✓	✓		✓	✓		
B	✓	✓	✓	✓	✓	✓	✓	✓
C	✓	✓	✓	✓	✓	✓	✓	✓
AB	✓	✓	✓	✓	✓	✓	✓	✓
AC	✓	✓			✓	✓	✓	✓
BC	✓	✓	✓	✓	✓	✓	✓	✓
ABC		✓	✓	✓				

3.3　General full factorial design

The experiment matrix containing coded factors and spectral emissivity measurements for the general ($2 \times 2 \times 2 \times 3$) factorial is shown in Table 6, while the ANOVA results are presented in Table 7. The general design is used to develop a mathematical model that specifically describes how the spectral emissivity varies over the detection wavelengths (1.6 μm, 2.1 μm, and 2.4 μm) of a commercial multi-wavelength pyrometer (Williamson PRO MWX-ST-17).

The percent contributions listed in the ANOVA (Table 7) indicate that the main effect of wavelength (D) is the most dominant, accounting for 69.8% of the total variability, followed by the Si/Mn ratio (B) and the dew point-Si/Mn (AB) interaction, which account for 13.7% and 9.6%, respectively. The combination of these three effects accounts for over 93% of the variations in the spectral emissivity. In addition, F-tests at 95% confidence interval (F-value $> F_{(0.05,1,32)} = 4.15$) indicate that 12 out of the 15 effects are statistically significant.

Table 6: The general $2 \times 2 \times 2 \times 3$ factorial design and spectral emissivity responses

Std. No.	Run No.	Coded Factors				Spectral emissivity, ε_λ	
		A	B	C	D	Replicate I	Replicate II
1	1	-1	-1	-1	-1.083	0.547	0.557
2	5	1	-1	-1	-1.083	0.644	0.638
3	3	-1	1	-1	-1.083	0.527	0.511
4	7	1	1	-1	-1.083	0.438	0.431
5	2	-1	-1	1	-1.083	0.485	0.499
6	6	1	-1	1	-1.083	0.561	0.571
7	4	-1	1	1	-1.083	0.502	0.506
8	8	1	1	1	-1.083	0.465	0.476
9	1	-1	-1	-1	0.167	0.375	0.383
10	5	1	-1	-1	0.167	0.461	0.456
11	3	-1	1	-1	0.167	0.385	0.371
12	7	1	1	-1	0.167	0.311	0.302
13	2	-1	-1	1	0.167	0.398	0.412
14	6	1	-1	1	0.167	0.455	0.464
15	4	-1	1	1	0.167	0.382	0.386
16	8	1	1	1	0.167	0.359	0.366
17	1	-1	-1	-1	0.917	0.308	0.312
18	5	1	-1	-1	0.917	0.370	0.365
19	3	-1	1	-1	0.917	0.326	0.313
20	7	1	1	-1	0.917	0.258	0.253
21	2	-1	-1	1	0.917	0.361	0.375
22	6	1	-1	1	0.917	0.408	0.416
23	4	-1	1	1	0.917	0.333	0.335
24	8	1	1	1	0.917	0.306	0.315

Table 7: ANOVA for the general ($2 \times 2 \times 2 \times 3$) factorial design

Source of variation	Sum of Squares ($\times 10^{-3}$)	Degree of Freedom	Mean Square ($\times 10^{-3}$)	F-value	p-value ($\times 10^{-3}$)	Percent Contribution	Significance at 95% CI
A	0.857	1	0.857	8.69	5.94	0.20	✓
B	57.83	1	57.8	585.94	3.84×10^{-19}	13.69	✓
C	1.77	1	1.77	17.98	0.178	0.42	✓
D	295	1	295	2987.95	3.55×10^{-30}	69.83	✓
AB	40.6	1	40.6	411.36	7.86×10^{-17}	9.61	✓
AC	0.643	1	0.643	6.51	15.7	0.15	✓
AD	0.1002	1	0.1002	1.02	321	0.02	
BC	2.07	1	2.07	20.95	0.0677	0.49	✓
BD	0.906	1	0.906	9.18	4.82	0.21	✓
CD	10.62	1	10.62	107.59	9.2×10^{-9}	2.51	✓
ABC	3.22	1	3.22	32.59	2.53×10^{-3}	0.76	✓
ABD	1.099	1	1.099	11.14	2.16	0.26	✓
ACD	0.0142	1	0.0142	0.14	707	3.37×10^{-3}	
BCD	4.53	1	4.53	45.87	1.18×10^{-4}	1.07	✓
ABCD	0.0123	1	0.0123	0.12	726	2.92×10^{-3}	
Error	3.16	32	0.0987			0.75	
Total	422	47					

3.3.1 *Regression analysis: spectral emissivity model*

The general expression for a linear regression model with interactions is given by

$$\hat{\varepsilon} = \beta_0 + \sum_{i=1}^{n}\beta_i x_i + \sum_{i=1}^{n-1}\sum_{j=2}^{n}\beta_{ij}x_i x_j + \sum_{i=1}^{n-2}\sum_{j=2}^{n-1}\sum_{k=3}^{n}\beta_{ijk}x_i x_j x_k + \cdots + \epsilon \tag{3}$$

where $\hat{y}$ is the predicted response; n is the number of factors; β_0, β_i, β_{ij}, and β_{ijk} are the unknown coefficients; x_i, x_j, and x_k are the factors (independent variables); and ϵ is the random error.

The full spectral emissivity model with all the independent variables and their two-, three-, and four-factor interactions is

$$\begin{aligned}
\hat{\varepsilon}_\lambda = {}& \beta_0 + \beta_1 A + \beta_2 B + \beta_3 C + \beta_4 D + \beta_{12}AB + \beta_{13}AC + \beta_{14}AD + \beta_{23}BC + \beta_{24}BD \\
& + \beta_{34}CD + \beta_{123}ABC + \beta_{124}ABD + \beta_{134}ACD + \beta_{234}BCD + \beta_{1234}ABCD
\end{aligned} \tag{4}$$

Table 8 shows the values of the coded regression coefficients, their standard error, and 95% confidence interval estimates for the full model. The standard errors for all model coefficients are dissimilar because the design is not orthogonal at the wavelength factor (D) due to the non-uniform spacing between the three detection wavelengths, as seen in Table 3. The uncoded coefficient values provided in Table 8 are obtained by substituting Eq. (2) for each factor associated with the model terms.

The model closely matches the experimental observations based on the small values of the sum-of-squares error and root-mean-square error, summarised in Table 8, as well as the adjusted R^2 of 0.989. Furthermore, the predictive ability of the model when faced with new factor levels is indicated by the prediction R^2 parameter; in this case, the prediction R^2 is equivalent to its adjusted R^2 which indicates good predictability for new observations within the current range of the factors.

Table 8: Regression coefficients for the spectral emissivity model

Model Term	Coefficient	Value	Standard Error	95% CI Low	95% CI High	Uncoded Coefficient Values
Intercept	β_0	0.41626	0.00143	0.41334	0.41918	1.32994
A	β_1	0.00423	0.00143	0.00131	0.00715	0.00554
B	β_2	-0.03471	0.00143	-0.03763	-0.03179	-2.16905
C	β_3	0.00608	0.00143	0.00316	0.00900	-0.73785
D	β_4	-0.09501	0.00174	-0.09856	-0.09147	-0.40820
AB	β_{12}	-0.02908	0.00143	-0.03200	-0.02616	-0.04035
AC	β_{13}	0.00366	0.00143	0.00074	0.00658	-0.00181
AD	β_{14}	-0.00175	0.00174	-0.00529	0.00179	-0.00129
BC	β_{23}	0.00656	0.00143	0.00364	0.00948	3.03408
BD	β_{24}	0.00527	0.00174	0.00173	0.00881	0.72351
CD	β_{34}	0.01803	0.00174	0.01449	0.02157	0.34865
ABC	β_{123}	0.00819	0.00143	0.00526	0.01111	0.02381
ABD	β_{124}	0.00580	0.00174	0.00226	0.00934	0.00893
ACD	β_{134}	-0.00066	0.00174	-0.00420	0.00288	0.00011
BCD	β_{234}	-0.01177	0.00174	-0.01531	-0.00823	-1.27151
ABCD	B_{1234}	-0.00061	0.00174	-0.00416	0.00293	-0.00323
Goodness-of-fit statistics						
SSE= 0.003158	RMSE = 0.009935	$R^2 = 0.992$	Adj. $R^2 = 0.989$	Pred. $R^2 = 0.984$		

The adequacy of the spectral emissivity model in Eq. (4) is further validated by analyzing the model residuals. The normal probability plot in Figure 5 (a) shows that the residual distribution is approximately normal with a slight skewness on the right tail. Although the residual vs predicted value plot in Figure 5 (b) does not have a pronounced non-random pattern, the distribution is not uniform around the zero-residual line. This could be due to heteroscedasticity (non-constant variance in the measurement) or a significant non-linear term missing from the model. The plot of the measured and predicted ε_λ at 1.6 μm to 2.4 μm in Figure 6 indicates that the trend in the residual

is most probably due to a quadratic relationship that was not accounted for. The slight curvature in the data can be better modelled by fitting a second-order model obtained with either a 3^k factorial design, central composite design (CCD), or the Box-Behnken design [26].
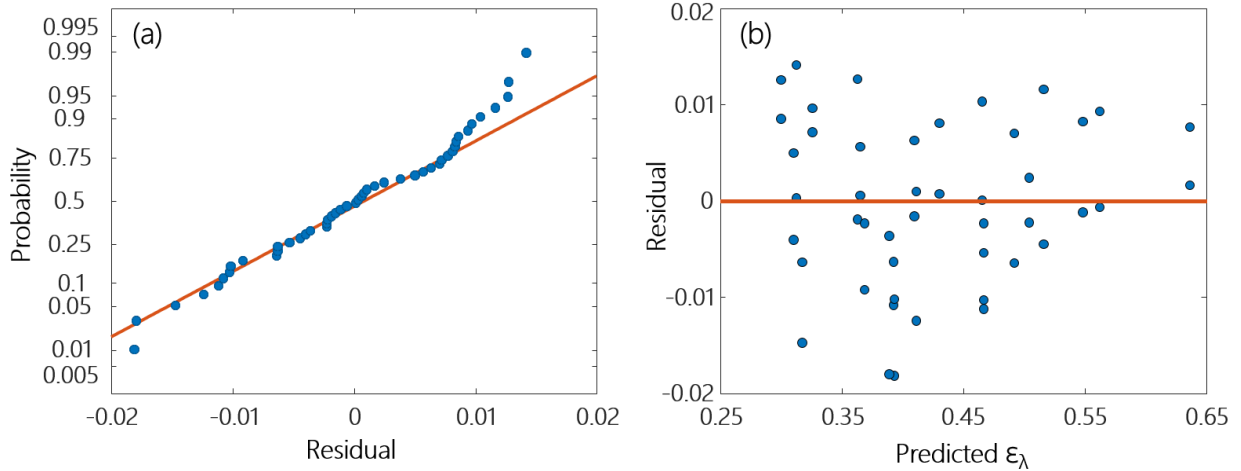

Figure 5. Residual analysis: (a) normal probability plot of residuals and (b) plot of residuals vs predicted spectral emissivity
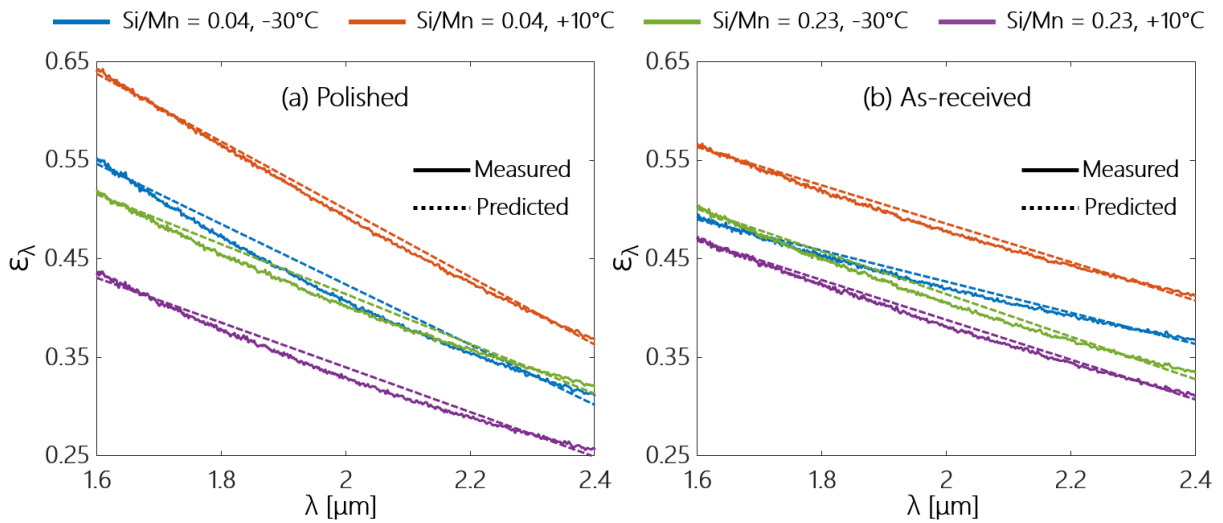

Figure 6. Comparison of measured and predicted spectral emissivity, ε_λ for (a) polished coupons and (b) as-received coupons.

Finally, we consider how the accuracy of the proposed model may be affected if the AHSS samples experience temperature-dependent emissivity variations associated with changing electron mobility at high temperatures. Typically, the Hagen-Rubens relation is used to predict how the radiative properties of metals might increase with temperature via its electrical conductivity [24, 38, 39]. However, the Hagen-Rubens relation is only valid for low-resistivity metals at longer wavelengths in the infrared region ($\lambda \gg 5\mu m$) [24, 38]. Also at shorter wavelengths, metals possess a "crossover wavelength" or "X-point" where the temperature effect is reversed, and the spectral emissivity decreases as temperature increases [24, 39]. These factors coupled with the effects of near-surface oxidation make it difficult to predict or isolate temperature-dependent emissivity variations for metal alloys observed at the shorter wavelengths critical to pyrometry. Metals exposed to high-temperature oxidizing environments, such as the annealing furnace, generally have radiative properties similar to those of their oxide layer, because most of the thermal emission is predominantly at shorter wavelengths where the interference effect of the oxide layer is even more significant [24, 39]. Previous pyrometry studies on steel alloys [7, 11] that have used *in situ* spectral emissivity measurements to determine the effect of temperature also indicate that variations observed at high temperatures are significantly influenced by the changes in surface properties due to oxidation. Given that our current *ex situ* characterization technique considers temperature-induced surface variations, additional *in situ* temperature-dependent emittance measurements will be required to accurately determine how the proposed AHSS spectral emissivity model performs with high-temperature pyrometry measurements. In addition to elucidating the temperature-dependence associated with changing electrical conductivity in the metal, further analysis will ensure that the derived model is directly applicable to industrial conditions.

4. Conclusion

To reduce the temperature-excursions produced by pyrometry errors during intercritical annealing, emissivity compensation algorithms must be derived that accurately represent how the spectral emissivity varies with material properties and annealing process parameters. This study uses the response surface methodology (RSM) to analyze and model spectral emissivity variations for dual-phase AHSS alloys in terms of dew point, silicon-to-manganese (Si/Mn) ratio, pre-annealed surface state, and wavelength. First, a 2^3 design shows how dew point, Si/Mn ratio and surface state interact to produce variations in the spectral emissivity at specific wavelengths between 1.2

μm – 4.0 μm. To develop a multivariate spectral emissivity model for multi-wavelength pyrometry measurements, these three factors are combined with wavelengths (1.6 μm, 2.1 μm, and 2.4 μm) in a general $(2 \times 2 \times 2 \times 3)$ factorial design.

ANOVA results for the 2^3 design identify the Si/Mn ratio (B), surface state (C), dew point-Si/Mn ratio interaction (AB), and Si/Mn ratio-surface state interaction (BC) to be statistically significant at each of the selected wavelengths. Their combined effect accounts for at least 93% of the total variability observed in the emissivity at these wavelengths. The main and interaction plots from this two-level design also indicate that polished samples have large emissivities at the shorter wavelengths ($\lambda = 1.2$ μm and $\lambda = 1.6$ μm), especially in the presence of the lower Si/Mn ratio.

Based on these results, a linear spectral emissivity model is then derived through regression analysis. The fitted model consists of all four main effects, five two-factor interactions, and three three-factor interactions. While the model closely interpolates the emissivity measurements, an analysis of the model residuals suggests the presence of one or more second-order effects that are not accounted for with the current model. A second-order emissivity model can easily be obtained using other RSM experiment designs such as 3^k factorial design, central composite design (CCD), or the Box-Behnken design [26], provided more samples are evaluated. The accuracy and reliability of the empirical model can also be further improved by using online high-temperature pyrometry measurements to investigate the presence of *in situ* temperature-dependent emissivity variations due to changing electron mobility in the metal.

The response surface methodology introduced in this paper provides key insights into how the evolving spectral emissivity of advanced high strength steels is influenced by process parameters during intercritical annealing, and the model derived from the RSM analysis will be used to provide more robust pyrometric temperatures, which are essential for the latest high performance alloys.

Appendix A: Visualizing the main effects from the 2^3 full factorial design

Main effect plots show how the average emissivity changes across the levels of a factor, independent of all other factors. The main effect plots for dew point (A), Si/Mn ratio (B), and pre-annealed surface state (C) are shown in Figures A.1- A.3, respectively. While the significant factors are identified through the ANOVA procedure, the slope of these plots offers further insights into how the spectral emissivity changes with the underlying factors.

For Factor A (dew-point) in Figures A.1 (a)-(h), increasing the factor level variable corresponds to an increase in the spectral emissivity except at 1.2 μm and 4.0 μm, where the opposite trend applies. The values on the dependent axis of each plot in Figures A.1 (a)-(h) show that the change in spectral emissivity due to the main effect of dew point (A) is quite small at each pyrometry detection wavelength. Figures A.2 (a)-(h) shows that an increase in Si/Mn ratio (B) corresponds to a decrease in emissivity at all wavelengths. For Factor C (surface state), Figures A.3 (a)-(h) show that the rougher as-received samples have the higher spectral emissivities except at the shortest wavelengths (1.2 μm and 1.6 μm), where the polished samples have higher spectral emissivities due to coherent interference of the uniformly structured oxide layer [32].
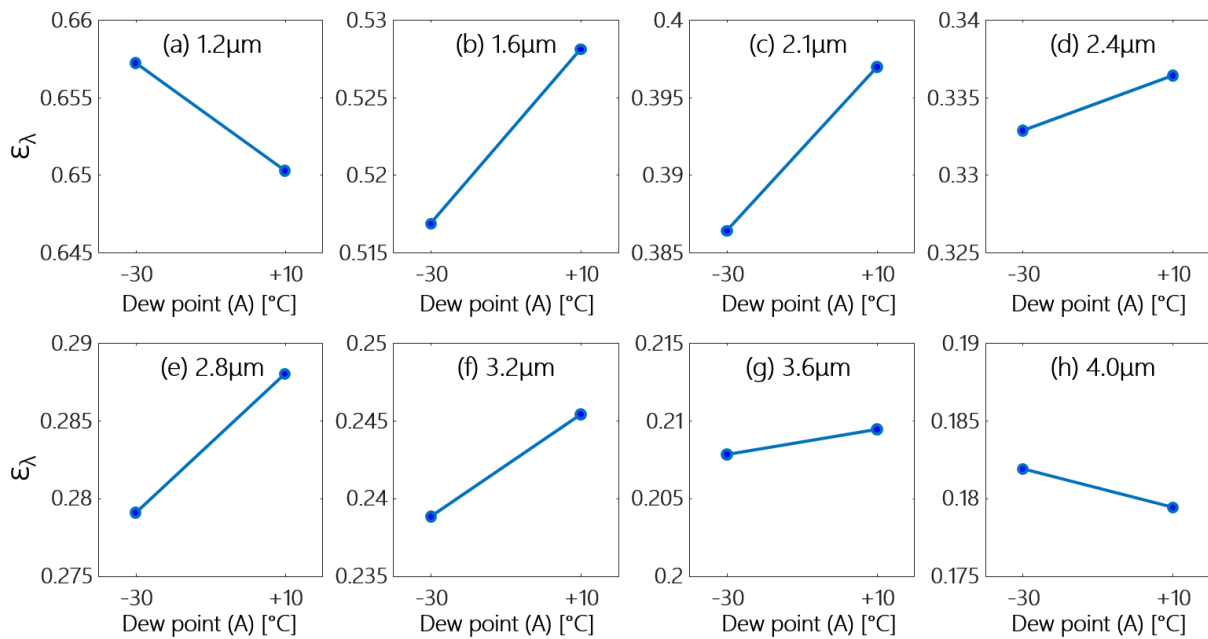
Figure A.1. Main effects plot for dew point (A) at the selected wavelengths: (a) 1.2 μm, (b) 1.6 μm, (c) 2.1 μm, (d) 2.4 μm, (e) 2.8 μm, (f) 3.2 μm, (g) 3.6 μm, and (h) 4.0 μm.
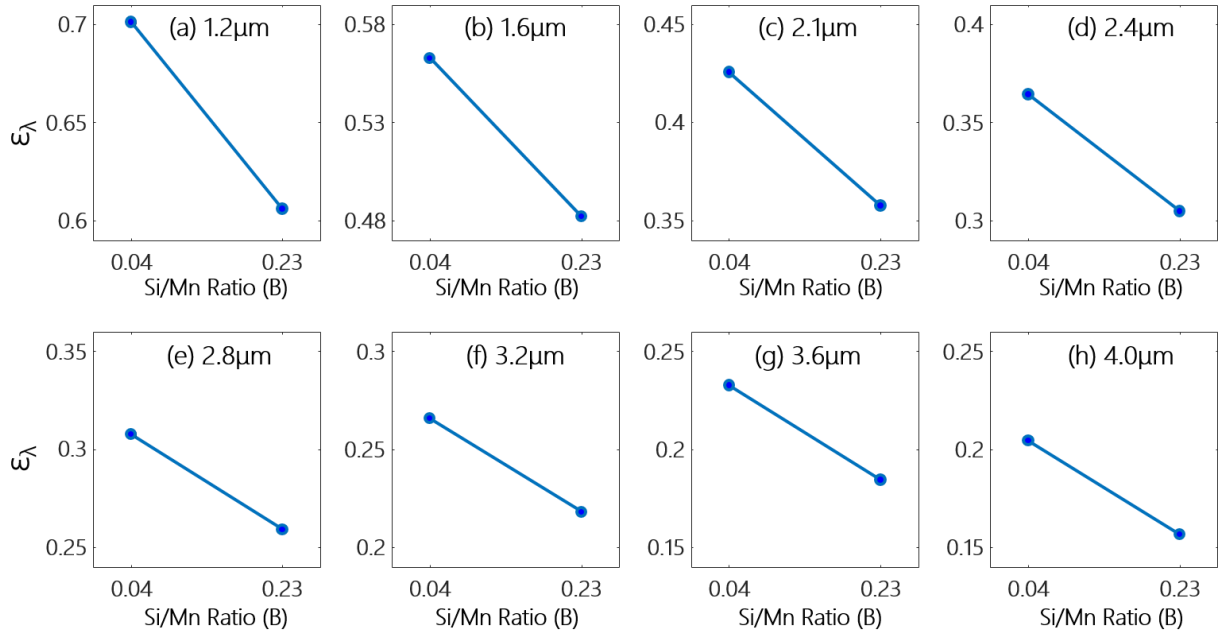
Figure A.2. Main effects plot for Si/Mn ratio (B) at the selected wavelengths: (a) 1.2 μm, (b) 1.6 μm, (c) 2.1 μm, (d) 2.4 μm, (e) 2.8 μm, (f) 3.2 μm, (g) 3.6 μm, and (h) 4.0 μm.
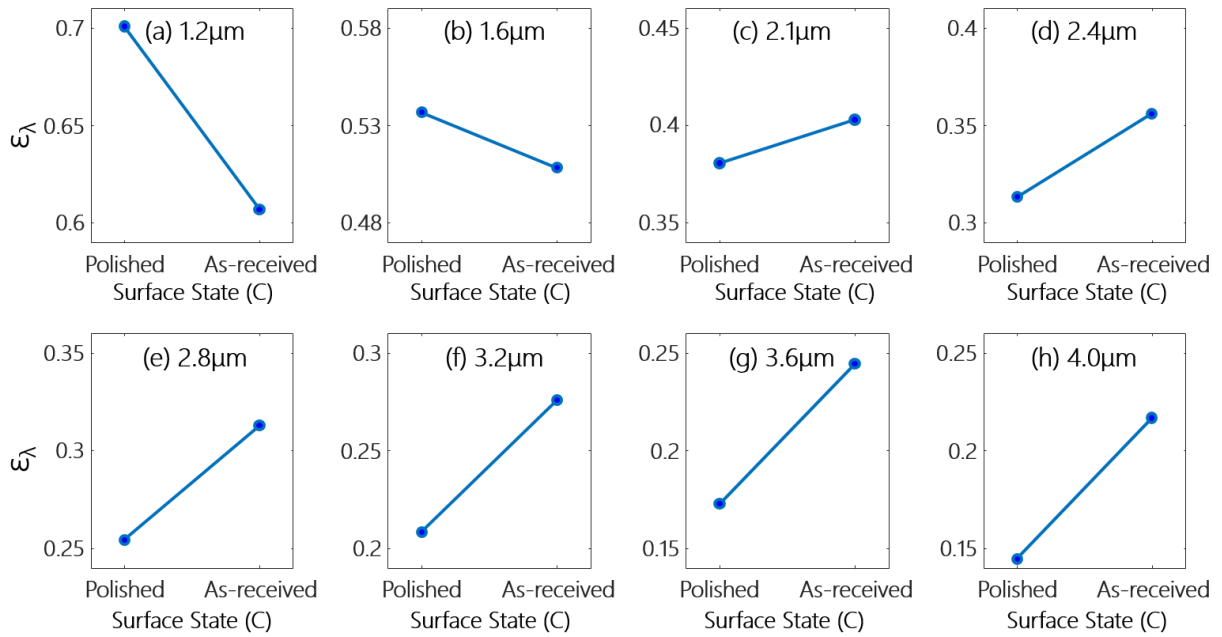
Figure A.3. Main effects plot for surface state (C) at the selected wavelengths: (a) 1.2 μm, (b) 1.6 μm, (c) 2.1 μm, (d) 2.4 μm, (e) 2.8 μm, (f) 3.2 μm, (g) 3.6 μm, and (h) 4.0 μm.

Appendix B: Visualizing the interaction effects from the 2^3 full factorial design

Figures B.1-B.3 illustrate the interaction effects for AB (dew point – Si/Mn ratio), AC (dew point – surface state), and BC (Si/Mn ratio – surface state), respectively. A two-factor interaction effect is defined as the average difference between the effect of one factor evaluated at the levels of the second factor [26]. Each interaction effect plotted in Figures B.1, B.2, and B.3 show the average spectral emissivity on the dependent axis against the levels of one factor for both levels of a second factor. Parallel lines (equal slopes) indicate that the first factor will produce the same rate of change in the response for both levels of the second factor, i.e. an insignificant interaction effect. For this reason, the stronger the interaction effect, the more non-parallel the lines become.

The AB interaction plotted in Figures B.1 (a)-(h) shows that for shorter wavelengths ($<$ 2.4 µm), the Si/Mn ratio of the steel has little effect at the lower dew point (-30°C) but produces a large positive effect when the Si/Mn ratio is reduced at the higher dew point. As the wavelength increases, there is a marked increase in the emissivity for samples of the lowest Si/Mn ratio even at the lower dew point (-30°C). The lines in Figures B.2 (a) – (h) are nearly parallel, indicating minimal interaction between dew point (A) and surface state (C) at these wavelengths. The spectral emissivity of both the polished and as-received samples is insensitive to dew point (A). The BC interactions plotted in Figures B.3 (a)-(h) appear to be strongest at 1.6 µm with the surface state (C) having little effect at the high Si/Mn ratio but a significant effect at the low Si/Mn ratio. At 2.1 µm and 2.4 µm, Figures B.3 (c) and (d), respectively, the lines appear to be parallel with similar slopes, which indicates that the interaction is not as strong at these wavelengths i.e. an increase in the Si/Mn ratio (B) will reduce the spectral emissivity irrespective of the pre-annealed surface state (C). At 3.6 µm and 4.0 µm, in Figures B.3 (g) and (h), respectively, an increase in the Si/Mn ratio (B) produces a decrease in the spectral for the as-received samples but a negligible effect on the spectral emissivity of the polished samples.

For the interaction effects involving the pre-annealed surface state (i.e. AC and BC), the polished samples exhibit higher spectral emissivity values at λ = 1.2 µm and λ = 1.6 µm, relative to the as-received samples. The increase in emissivity with reducing surface roughness for the AC and BC interactions at these wavelengths contributes to the negative slope observed in the main effect plots for the surface state (C) in Figures A.3 (a) and (b).
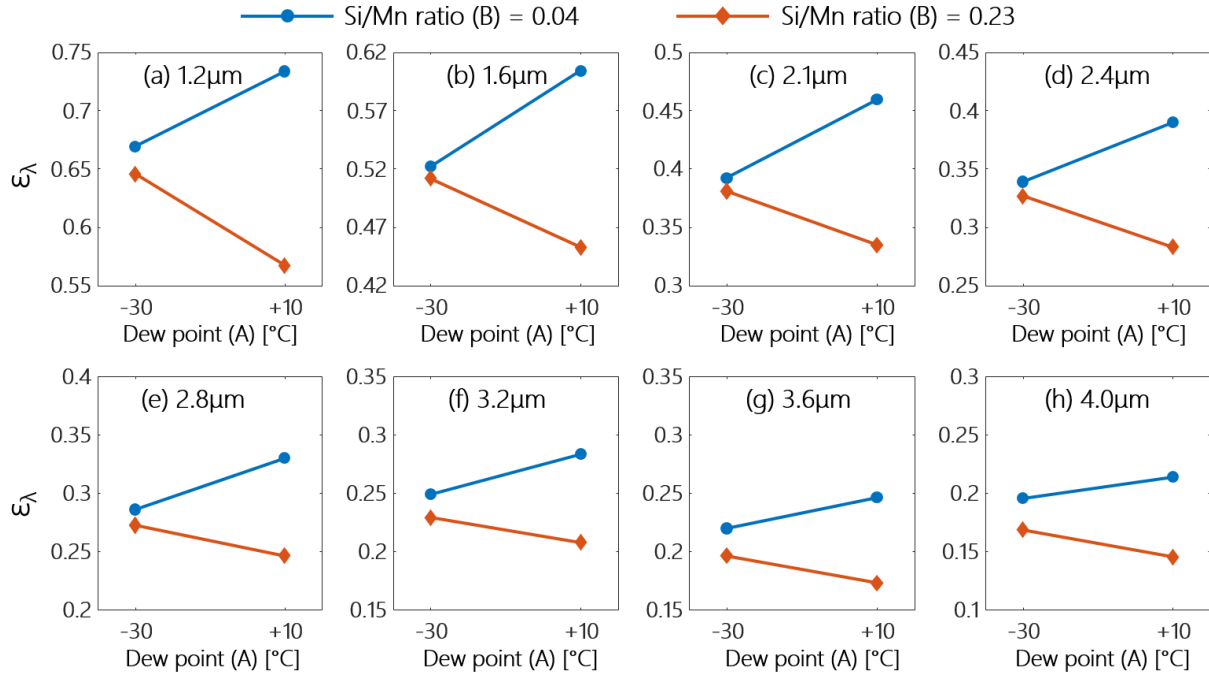
Figure B.1. Interaction plot for dew point - Si/Mn ratio (AB) at the selected wavelengths: (a) 1.2 μm, (b) 1.6 μm, (c) 2.1 μm, (d) 2.4 μm, (e) 2.8 μm, (f) 3.2 μm, (g) 3.6 μm, and (h) 4.0 μm.
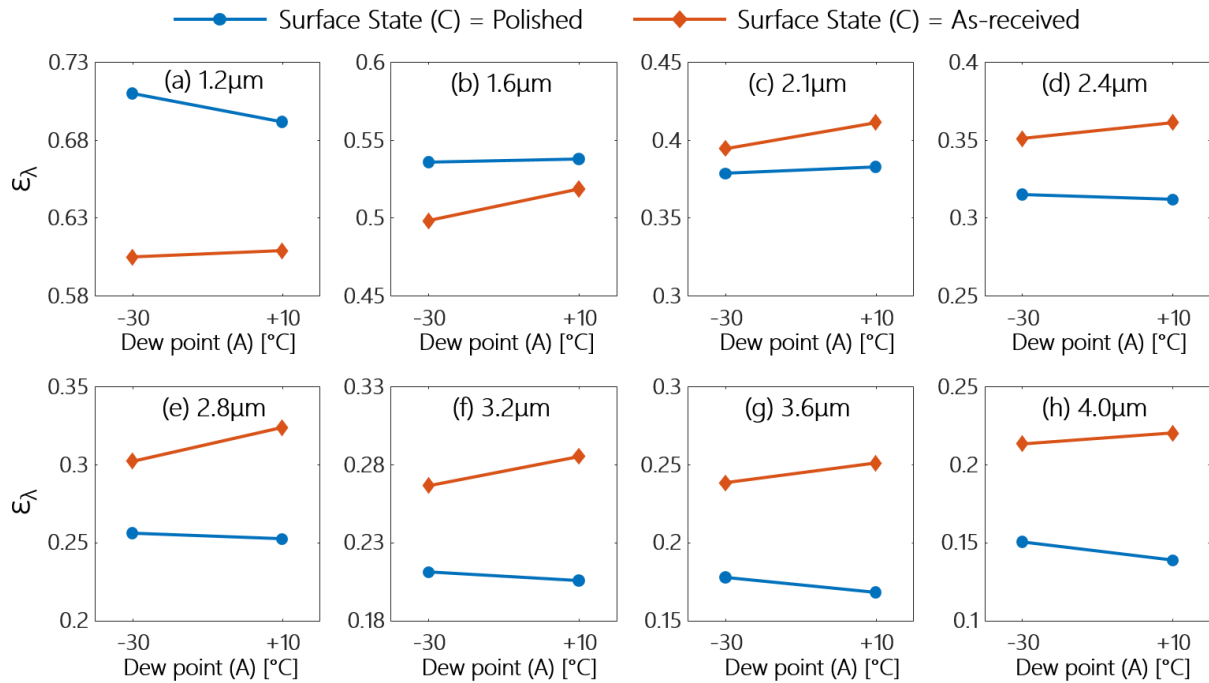

Figure B.2. Interaction plot for dew point - surface state (AC) at the selected wavelengths: (a) 1.2 μm, (b) 1.6 μm, (c) 2.1 μm, (d) 2.4 μm, (e) 2.8 μm, (f) 3.2 μm, (g) 3.6 μm, and (h) 4.0 μm.
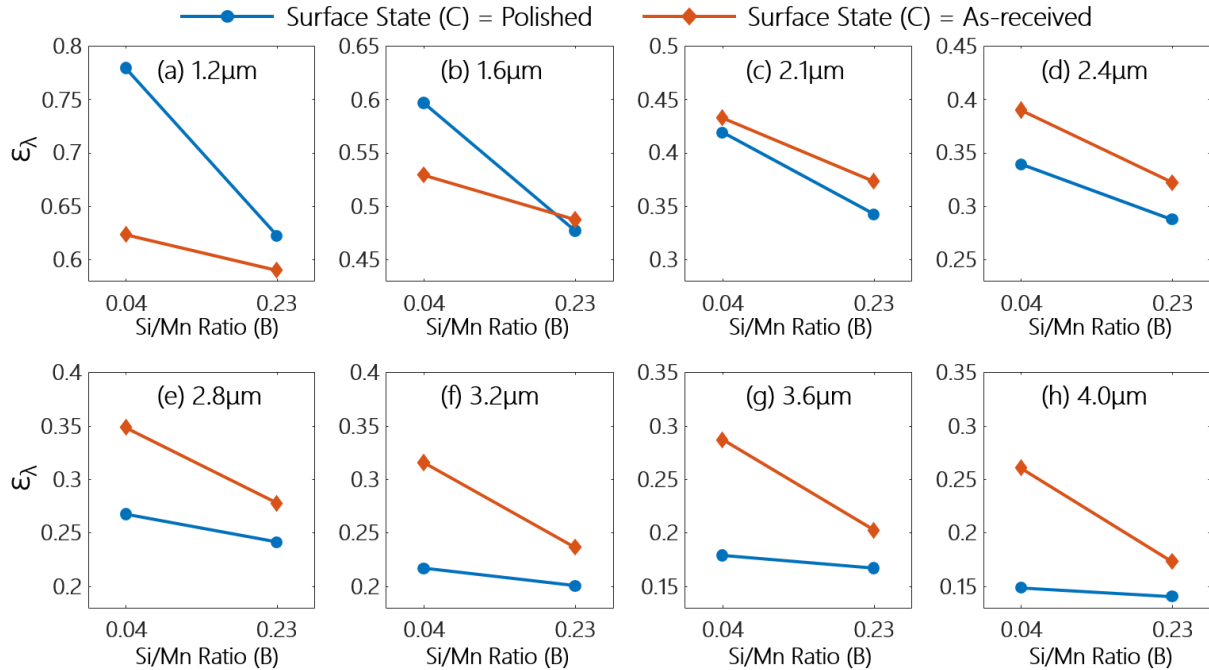
Figure B.3. Interaction plot for Si/Mn ratio - surface state (BC) at the selected wavelengths: (a) 1.2 μm, (b) 1.6 μm, (c) 2.1 μm, (d) 2.4 μm, (e) 2.8 μm, (f) 3.2 μm, (g) 3.6 μm, and (h) 4.0 μm.

Acknowledgement

Supplementary Materials

Supplementary material associated with this paper can be found, in the online version, at doi: XXX

References

[1]   B.K. Tsai, D.P. Dewitt, G.J. Dail, Application of dual-wavelength radiation thermometry to the aluminum industry, Measurement, 11 (3) (1993) 211-221.

[2]   R. Usamentiaga, D. F. García, J. Molleda, F. G. Bulnes, J. M. Pérez, Temperature measurement using the wedge method: comparison and application to emissivity estimation and compensation, IEEE Trans. Instrum. Meas. 60 (5) (2011) 1768–1778.

[3]   F. Tanaka, D.P. Dewitt, Theory of a new radiation thermometry method and an experimental study using galvannealed steel specimens, Trans. Soc. Instrum. Control Eng. 25 (10) (1989) 1031–1037.

[4]   B. K. Tsai, R. L. Shoemaker, D. P. DeWitt, B. A. Cowans, Z. Dardas, W. N. Delgass, G. J. Dail, Dual-wavelength radiation thermometry: emissivity compensation algorithms, Int. J. Thermophys. 11 (1) (1990) 269–281.

[5]   R.G. Thiessen, E. Bocharova, D. Mattissen, R. Sebald, Temperature measurement deviation during annealing of multiphase steels, Metall. Mater. Trans. B, 41 (4) (2010) 857–863.

[6]   C.-D. Wen, Investigation of steel emissivity behaviors: examination of multispectral radiation thermometry (MRT) emissivity models, Int. J. Heat Mass Transfer 53 (9) (2010) 2035–2043.

[7]   A. Araújo, Multi-spectral pyrometry—a review, Meas. Sci. Technol. 28 (8) (2017) 082002.

[8]   M.A. Khan, C. Allemand, T.W. Eagar, Noncontact temperature measurement. I. interpolation based techniques, Rev. Sci. Instrum. 62 (2) (1991) 392–402.

[9]   M.A. Khan, C. Allemand, T.W. Eagar, Noncontact temperature measurement. II. least squares based techniques, Rev. of Sci. Instrum. 62 (2) (1991) 403–409.

[10]   M.A. Pellerin, D.P. DeWitt, G.J. Dail, Multispectral radiation thermometry for aluminum alloys, in: T.L. Bergman, D.A. Zumbrunnen, Y. Bayazitoglu, A.G. Lavine (Eds.), Heat Transfer in Metals and Containerless Processing and Manufacturing, ASME HTD, 162 (1991) 43–47.

[11]   M.A. Pellerin, Multispectral radiation thermometry for industrial applications, PhD thesis, Purdue University, West Lafayette, IN, 1999.

[12]   Th. Duvaut, D. Georgeault, J.L. Beaudoin, Multiwavelength infrared pyrometry: optimization and computer simulations. Infrared Phys. Techn. 36 (7) (1995) 1089–1103.

[13]   E. Hagen, H. Rubens, Über Beziehungen des Reflexions- und Emissionsvermögens der Metalle zu ihrem elektrischen Leitvermögen, Ann. Phys. 316 (8) (1903) 873–901.

[14]   S.H. Ham, C. Carteret, J. Angulo, G. Fricout, Relation between emissivity evolution during annealing and selective oxidation of TRIP steel, Corros. Sci. 132 (2018) 185–193.

[15]   Q. Somveille, P. Mosser, M. Brochu, K.J. Daun, Effect of oxidation on emissivity for DP780 and DP980 steels, in: Proceedings of Eleventh International Conference on Zinc and Zinc Alloy Coated Steel Sheet, Tokyo, Japan, 2017, pp. 210–217.

[16]   T. Iuchi, T. Furukawa, S. Wada, Emissivity modeling of metals during the growth of oxide film and comparison of the model with experimental results, Appl. Opt. 42 (13) (2003) 2317–2326.

[17]   C.-D. Wen, I. Mudawar, Modeling the effects of surface roughness on the emissivity of aluminum alloys, Int. J. Heat Mass Transfer 49 (23-24) (2006) 4279–4289.

[18]   S.G. Agababov, Effect of secondary roughness on the emissive properties of solid bodies, Teplofizika Vysokikh Temperatur 8 (1) (1970) 220–222.

[19]   J.L. King, H. Jo, S.K. Loyalka, R.V. Tompson, K. Sridharan, Computation of total hemispherical emissivity from directional spectral models, Int. J. Heat Mass Transfer 109 (C) (2017) 894–906.

[20]   H. Jo, J.L. King, K. Blomstrand, K. Sridharan, Spectral emissivity of oxidized and roughened metal surfaces, Int. J. Heat Mass Transfer 115(PB) (2017) 1065–1071.

[21]   K. Lin, K.J. Daun, Interpreting the spectral reflectance of advanced high strength steels using the Davies' model, J. Quant. Spectrosc. Radiat. Transfer 242 (2020).

[22]   H. Davies, The reflection of electromagnetic waves from a rough surface, in: Proceedings of the IEE - Part IV: Inst. Monogr. 101 (7) (1954) pp. 209–214.

[23]   L. Chen, R. Fourmentin, J. Mc Dermid, Morphology and kinetics of interfacial layer formation during continuous hot-dip galvanizing and galvannealing, Metall. Mater. Trans. A 39 (9) (2008) 2128–2142.

[24] J. R. Howell, R. Siegel, M. P. Mengüç, thermal radiation heat transfer, 5th ed., CRC Press, Boca Raton, FL, 2015.

[25] Standard ASTM A1079-17, 2017.

[26] D.C. Montgomery, Design and analysis of experiments, 8th ed., John Wiley & Sons, Hoboken, NJ, 2013.

[27] A. Witek-Krowiak, K. Chojnacka, D. Podstawczyk, A. Dawiec, K. Pokomeda, Application of response surface methodology and artificial neural network methods in modelling and optimization of biosorption process, Bioresour. Techn. 160 (2014) 150–160.

[28] R. Elemuren , R. Evitts, I.N.A. Oguocha, G. Kennell, R. Gerspacher A. G. Odeshi, Full factorial, microscopic and spectroscopic study of erosion-corrosion of AISI 1018 steel elbows in potash brine-sand slurry, Tribol. Int. 142 (2020) 105989.

[29] A.V. Veličković, O.S. Stamenković, Z.B. Todorović, V. B. Veljković, Application of the full factorial design to optimization of base-catalyzed sunflower oil ethanolysis, Fuel 104 (2013) 433–442.

[30] A. Srinivasan, T. Viraraghavan, Oil removal from water by fungal biomass: A factorial design analysis. J. Hazard. Mater. 175 (1) (2010) 695–702.

[31] J.A. Ogilvy, Wave scattering from rough surfaces, Rep. Prog. Phys. 50 (12) (1987) 1553–1608.

[32] R. R. Brannon Jr., R.J. Goldstein, Emittance of Oxide Layers on a Metal Substrate, ASME. J. Heat Transfer 92(2) (1970) 257–263.

[33] S. Uran, B. Veal, M. Grimsditch, J. Pearson, A. Berger, Effect of surface roughness on oxidation: changes in scale thickness, composition, and residual stress, Oxid. Metals 54 (1-2) (2000) 73–85.

[34] P. Mosser, Q. Somveille, K.J. Daun, M. Brochu, Effect of temperature deviation during critical annealing of HSLA and DP980 steels, in: Proceedings of Eleventh International Conference on Zinc and Zinc Alloy Coated Steel Sheet, Tokyo, Japan, 2017, pp. 218–225.

[35] Y.A. Chang, W.A. Oates, Materials thermodynamics, Vol. 7, John Wiley & Sons, 2010.

[36]   M. Pourmajidian, J. McDermid, Selective oxidation of a 0.1C-6Mn-2Si third generation advanced high-strength steel during dew-point controlled annealing, Metall. Mater. Trans. A 49 (5) (2018) 1795–1808.

[37]   Y. Suzuki, T. Yamashita, Y. Sugimoto, S. Fujita, S. Yamaguchi, Thermodynamic analysis of selective oxidation behavior of Si and Mn-added steel during recrystallization annealing, ISIJ Int. 49 (4) (2009) 564–573.

[38]   D.P. DeWitt and J.C. Richmond, Thermal Radiative Properties of Materials, Theory and Practice of Radiation Thermometry, in: D.P. DeWitt, G.D. Nutter (Eds.), John Wiley and Sons, New York, 1988, pp. 130–135.

[39]   M.F. Modest, Radiative heat transfer, 3rd ed., Academic Press, New York, 2013.

Development of a multivariate spectral emissivity model for an advanced high strength steel alloy through factorial design-of-experiments

Fatima K. Suleiman*, Kaihsiang Lin, Kyle J. Daun

Department of Mechanical and Mechatronics Engineering, University of Waterloo

200 University Avenue West, Waterloo, Ontario N2L 3G1, Canada

Declaration of interests

☒ The authors declare that they have no known competing financial interests or personal relationships that could have appeared to influence the work reported in this paper.

☐ The authors declare the following financial interests/personal relationships which may be considered as potential competing interests:

Development of a multivariate spectral emissivity model for an advanced high strength steel alloy through factorial design-of-experiments

Fatima K. Suleiman*, Kaihsiang Lin, Kyle J. Daun

Department of Mechanical and Mechatronics Engineering, University of Waterloo

200 University Avenue West, Waterloo, Ontario N2L 3G1, Canada

Author Statement

*Corresponding author: fsuleiman@uwaterloo.ca

Supplementary Material

Click here to access/download
Supplementary Material
SupplementaryMaterial_Suleiman_etal_JQSRT_2021.xls
x